Velocity profiles measured for airflow through a large-scale model of the human nasal cavity

INTAEK HAHN, PETER W. SCHERER, AND MAXWELL M. MOZELL
Department of Bioengineering, University of Pennsylvania, and Monell Chemical Senses Center, Philadelphia, Pennsylvania 19104; and Department of Physiology, State University of New York Health Science Center, Syracuse, New York 13210

HAHN, INTAEK, PETER W. SCHERER, AND MAXWELL M. MO-ZELL. *Velocity profiles measured for airflow through a large-scale model of the human nasal cavity.* J. Appl. Physiol. 75(5): 2273–2287, 1993.—An anatomically accurate, ×20 enlarged scale model of a healthy right human adult nasal cavity was constructed from computerized axial tomography scans for the study of nasal airflow patterns. Detailed velocity profiles for inspiratory and expiratory flow through the model and turbulence intensity were measured with a hot-film anemometer probe with 1 mm spatial resolution. Steady flow rates equivalent to 1,100, 560, and 180 ml/s through one side of the real human nose were studied. Airflows were determined to be moderately turbulent, but changes in the velocity profiles between the highest and lowest flow rates suggest that for normal breathing laminar flow may be present in much of the nasal cavity. The velocity measurements closest to the model wall were estimated to be inside the laminar sublayer, such that the slopes of the velocity profiles are reasonably good estimates of the velocity gradients at the walls. The overall longitudinal pressure drop inside the nasal cavity for the three inspiratory flow rates was estimated from the average total shear stress measured at the central nasal wall and showed good agreement with literature values measured in human subjects.

nasal airflow, nasal pressure drop, nasal resistance, airway turbulence, olfactory airflow

THE HUMAN NASAL CAVITY plays an important role in the respiratory system by warming, humidifying, and cleaning the inspired air (24). During this process, however, it becomes a potential target for inhaled air pollutants and toxins that can cause various lesions in the nasal mucosa (13, 16, 17). The nose is also the site of olfaction in which odorant molecules contained in the inspired air contact the olfactory mucosa in the roof of the nasal cavity (olfactory slit) (1, 10, 14, 22). Airflow patterns in the nasal cavity strongly affect the uptake and deposition of inhaled pollutants, air-borne particles, and odorants over the entire nasal mucosa (13). Investigation of nasal velocity profiles provides important information necessary to characterize all nasal airway transport processes.

Early attempts to determine human nasal airflow patterns involved in vivo observations of the distribution of air-borne powder (7, 15, 19). These observations often provided conflicting and uncertain results because of the small size and complex anatomy of the nasal cavity. In early in vitro studies, Proetz (18), Stuiver (22), Masing (11), and Swift and Proctor (24) studied nasal airflow patterns with the use of smoke and water flowing through life-size models of the human nasal cavity made from nasal casts, with a clear flat plastic plate replacing the septum for visual observation. Proetz observed that most of the incoming air is drawn through the middle meatus. Stuiver reported that 5–20% of inspired air passes through the olfactory slit, depending on the total steady flow rate entering through the external naris of the model, and Masing demonstrated that the flow pattern is a function of the location in the nostril where the dye stream is released. Swift and Proctor mapped out the velocity field of the inspiratory nasal airflow with a pitot tube and indicated recirculating eddy currents in the superior nose of the model they used. In a more recent in vitro study, Girardin et al. (6) used laser anemometry to measure the velocity of water droplets in air as this suspension flowed through a life-size model of the human nasal cavity. This technique allowed the detailed velocity fields seen during the inhalation of water particles to be mapped out quantitatively, but a flat plastic plate had to be used in place of the real nonplanar nasal septum. Also, this study investigated nasal airflow with only one flow rate of 167 ml/s, and more studies using different flow rates are desirable.

An anatomically correct actual size nasal cavity model was used by Hornung et al. (8), and nasal airflow patterns were investigated by studying the flow of radioactive xenon through the model. This study confirmed the general results of previous studies done by Masing (11) and Stuiver (22) in that air flowing along the lateral side of the nasal fossa was somewhat more directed toward the olfactory area and increasing the flow rate increased the percentage of incoming stimulus directed toward the olfactory slit. However, the small size of the model made it difficult to study detailed flow patterns in localized regions.
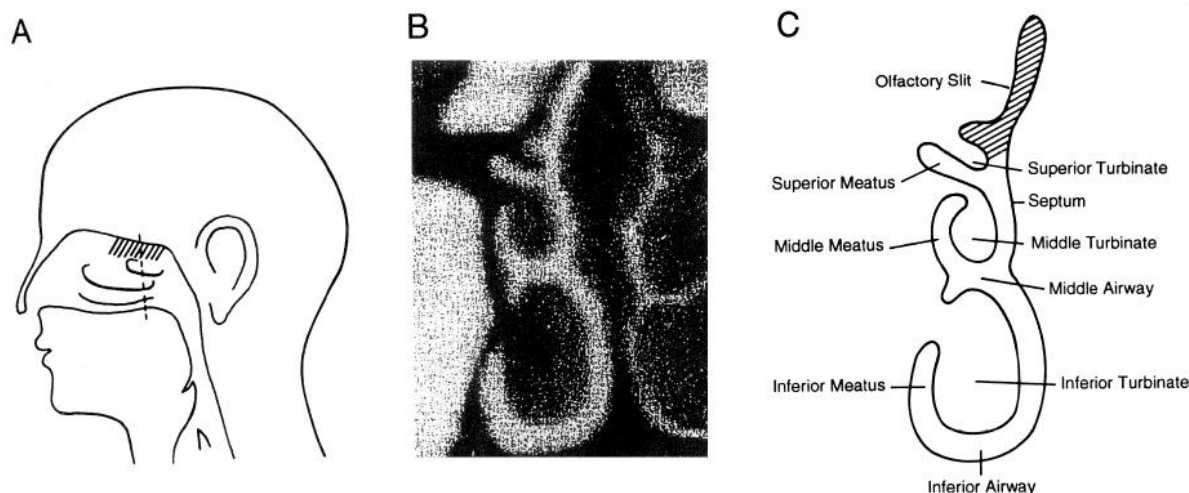
A

B

C

FIG. 1. *A*: human nasal cavity. Hatched area, olfactory region. *B*: computerized axial tomography (CAT) scan of cross section (dashed line in *A*) of nasal cavity. *C*: sections of human nasal airway. Hatched area, olfactory region.

MATERIALS AND METHODS

Major obstacles in studying detailed airflow patterns through the human nasal cavity are its small size and complicated anatomy. To overcome these difficulties, a scaled-up physical model was constructed. By applying fluid mechanical scaling principles, airflow through the model was created to be kinematically similar to that in the real human nose.

A large scale ($\times 20$) anatomically correct model of a human adult right nasal cavity from the tip of the naris to the beginning of the nasopharynx was constructed from computerized axial tomography (CAT) scans of a healthy male nasal cavity as follows (Fig. 1). *1)* Coronal CAT scans were taken 2 mm apart along the nasal cavity of a living human subject. The CAT scans were examined by a rhinologist and were determined to represent a "normal" healthy human nasal cavity. *2)* The outlines of these cross sections were enlarged $\times 20$ using photographic and pantographic enlargement techniques and were traced on Styrofoam insulation slabs that were 61 cm wide, 122 cm long, and 4 cm thick. *3)* The tracings were cut out of the Styrofoam slabs, and the slabs were then glued together serially to produce a large Styrofoam block ($\sim 169 \times 61 \times 122$ cm) with the nasal airway as a tortuous channel through it. *4)* The block was carefully cut into several sections that can be disassembled and reassembled easily in such a way that all parts of the interior surface are accessible. *5)* The surface of the interior cavity on each section was coated and smoothed with casting plaster. *6)* Eighty-five holes were drilled through the sides of the block to allow the insertion of a hot-film anemometer probe (TSI model 1269A) to measure velocities of the air flowing inside the model. The locations of the holes were chosen so that velocity measurements could be made throughout the nasal cavity, including the naris; the anterior, middle, and posterior sections of the turbinate region; and the olfactory cleft. When not in use, the holes were blocked by airtight cork stoppers. Figure 2 shows the locations of the planes and their corresponding cross sections in the human nasal cavity on which velocity measurements were taken. *Plane 1*

corresponds to the external naris, and *plane 2* corresponds to the posterior section of the nasal valve region. *Plane 3* represents the anterior part of the inferior and middle turbinate region, and *planes 4* and *5* represent the superior turbinate region and the beginning of the nasopharynx, respectively. Nine holes (1 cm diam) were drilled along *planes 1* and *5,* and 15 holes were drilled along *planes 2, 3,* and *4*. These holes were evenly distributed along these planes, and 14 extra holes (6 in *plane 6*) were made, as shown in Fig. 2, in the olfactory region. *7)* Nasal hairs (vibrissae) were simulated on some of the experimental runs by 1-mm-diam copper rods, cut to be 20 times longer than the real nasal hairs, and "planted" around the external naris of the model. *8)* Airflow through the model was produced by a brushless direct current fan (Panaflo model FBH 12G24M) placed in a flexible 183-cm-long, 45-cm-diam cylindrical aluminum foil duct at the nasopharyngeal end of the model (Fig. 3*A*). Both inspiratory and expiratory airflows were produced by changing the flow direction of the fan.

Airflow through the nasal model was designed to be kinematically similar to that occurring in the real human nasal cavity by matching the numerical values of the relevant dimensionless numbers that characterize the flow. For bulk flow (momentum transport) study, the equations of motion for a Newtonian fluid show that it is necessary to consider only the Reynolds number

$$\text{Re} = \frac{\bar{u}d}{\nu} \qquad (1)$$

and the Womersley frequency parameter

$$\alpha = d \sqrt{\frac{2\pi\omega}{\nu}} \qquad (2)$$

where $\bar{u}$ is the mean local air velocity, d is a local diameter of the nasal airway, ν is the kinematic viscosity of air, and ω is the breathing frequency. The local diameter of the nasal airway used in this paper is the cross-sectional distance between the nasal walls at a given measurement site, which was determined from CAT scans. The cross-sectional areas and perimeters for the six planes chosen
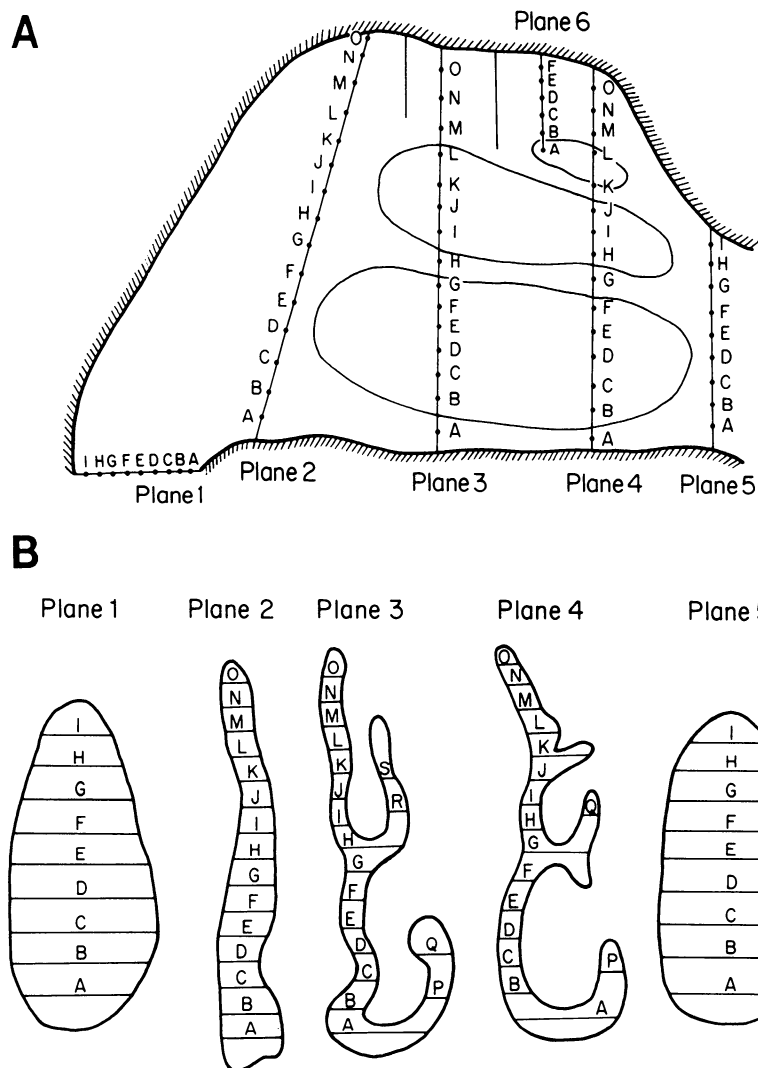
FIG. 2. Velocity measurement sites in nasal model: side view (*A*) and corresponding cross sections of *plane 1* (naris), *plane 2, plane 3, plane 4,* and *plane 5* (*B*). Alphabetized lines, velocity measurement trajectories.

for velocity measurement were also determined from the CAT scans. Data for the local diameter, area, and perimeter are presented in Table 2 in APPENDIX A.

Because d in the scaled-up model is 20 times larger than d in the real nasal cavity while ν is the same in both, to match the Re values, it is necessary to produce a gas flow through the physical model such that $\bar{u}$ within the model is 20 times smaller than that within the real hu-
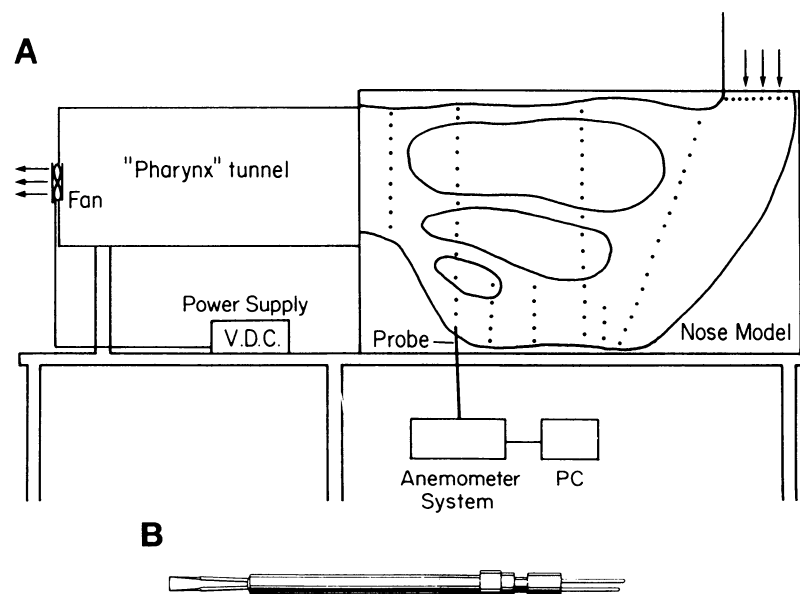

FIG. 3. *A*: experimental setup. Measurement holes are indicated by dots on side of model. Both inspiratory and expiratory nasal airflows can be produced by changing direction of fan. PC, personal computer; VDC, voltage, direct current. *B*: hot-film anemometer probe.
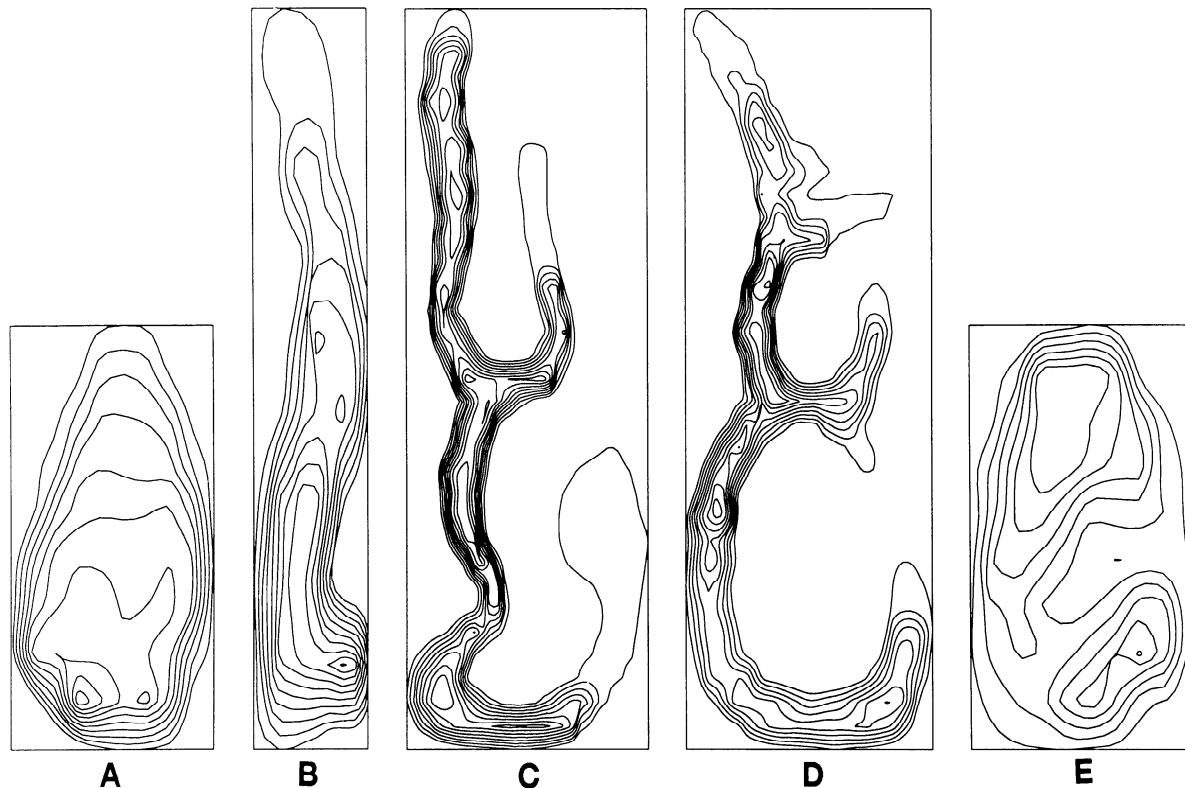
FIG. 4. Isospeed contour maps for medium inspiratory nasal airflow. All speeds are normalized by highest value (U_0 = 8.8 m/s) measured at naris for given flow rate, and distance between lines represents 10% of U_0. A, plane 1; B, plane 2; C, plane 3; D, plane 4; E, plane 5.

man nasal cavity. Also, because gas volume flow rate, $\dot{Q}$, through the nose is proportional to $\bar{u}d^2$, it follows that $\dot{Q}_{model} = 20 \times \dot{Q}_{nose}$ when Re is matched in both systems. The transit time, T, required for odorants to be convected by the flow between the external nares and the olfactory region is proportional to the transit path length divided by the velocity: therefore, $T_{model} = 400 \times T_{nose}$. In a similar way α is matched when ω or frequency of sniffing in the physical model is only 1/400 of that occurring in the real nose. Flows that occur in a short time in the real nasal cavity (e.g., sniffing) will last considerably longer in the scaled-up model. Indeed, physiological flows in the real nose can usually be well approximated as steady-state flows in the scaled-up model (see DISCUSSION). The time response of the instruments needed to measure flow velocity can also be much slower in the large model than in the real nose. Another advantage of the scaled-up model is the possibility of far more detailed studies of the flow patterns inside the nasal cavity due to the ease with which anemometer probes can be introduced into the larger flow spaces.

The hot-film anemometer probe (model 1269A, TSI, St. Paul, MN; Fig. 3B) was inserted through one of the measurement holes and advanced across the interior air space to obtain the velocity profiles. By changing the power output of the direct current power supply, the fan was adjusted to produce airflow rates that were equivalent to 1,100, 560, and 180 ml/s in the real nose. The flow rates selected correspond to a forceful sniff, medium sniff, and average breathing rate, respectively, for an adult human. These flow rates are often given for the combination of both nasal cavities, but because it is well

documented (5) that most adult humans experience "the nasal cycle" (a 3- to 4-h cycle of alternation of patency between the nasal cavities), these rates may also be applied to one side of the nose only. To make sure that any noise from the fan does not influence airflow patterns inside the nasal cavity model, time-dependent velocity measurements were obtained for airflow generated by the fan when detached from the model (see Fig. 13, A and C, in APPENDIX B). These measurements show very quiet time-dependent velocity traces with a few low-frequency random fluctuations for both high and low flow rates. When they are compared with the time-dependent inspiratory velocity measurements made inside the nasal cavity model (see Fig. 13, B and D, in APPENDIX B), it is apparent that the velocity measured inside the model exhibits considerably higher frequency and more intense random fluctuations than those measured in front of the fan alone. This supports the contention that noise caused by the fan's vibration does not have a significant effect on the turbulence or random fluctuations in the airflow inside the nasal cavity model and also supports the conclusion that the random fluctuations of velocity seen in nasal airflow are caused mostly by the complex anatomy of the nasal airway.

The anemometer probe (Fig. 3B) used for the velocity measurements is a hot-film sensor, 0.025 mm wide and 1 mm long, attached to a quartz rod with a 1.5 mm diam. During insertion, the probe was placed in a cylindrical stainless steel tube that guided and protected it while it traversed the wall of the model. The velocity measurements were taken along the traversing line at increments of 1–5 mm (equivalent to 0.05–0.25 mm in the real nose),
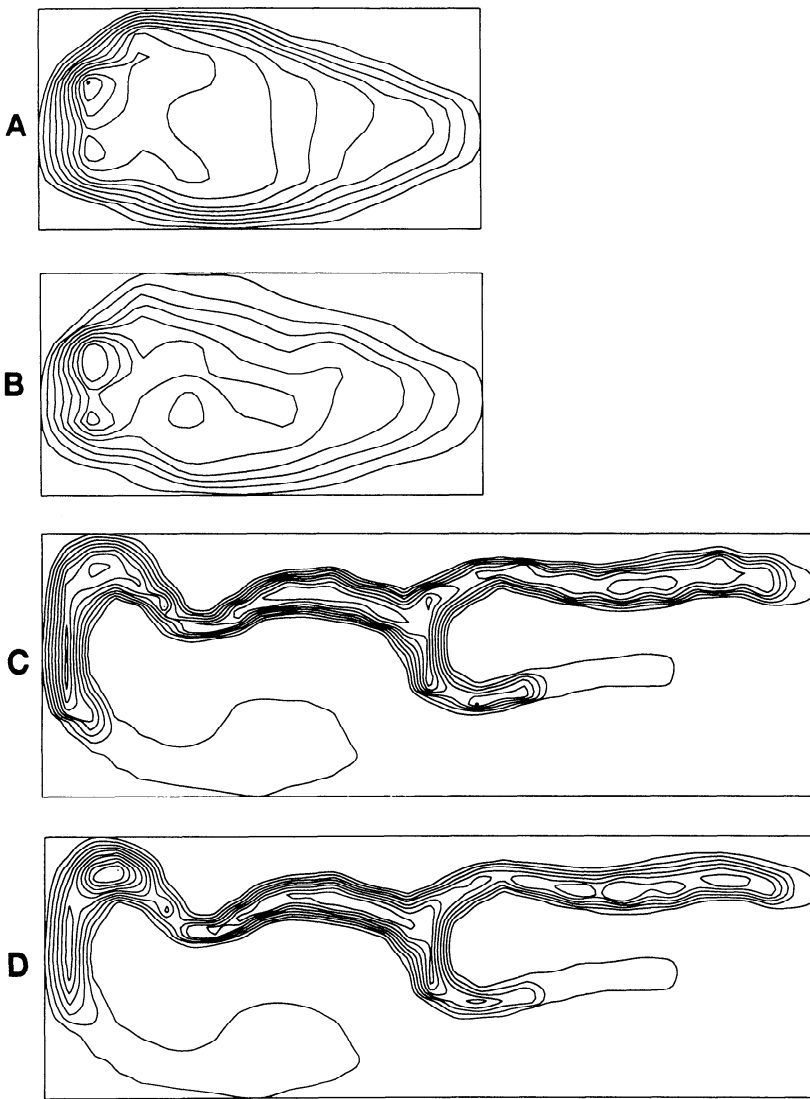
depending on the total width of the particular cross section. The procedure was repeated at all measurement sites. The small size of the probe and the large size of the model made it possible to obtain a sufficient number of measurements for adequate mapping of the velocity profiles at even the narrowest sections of the nasal passages. For the two higher flow rates of 1,100 and 560 ml/s, velocity measurements could be obtained at points within 1.5 mm from the walls (0.075 mm in the real nose). For the low flow rate (180 ml/s) some of the velocities near the nasal wall were too low for the probe to detect, but it was still possible to obtain velocity measurements at points as close as 5 mm from the wall (0.25 mm in the real nose).

The hot-film anemometer probe was calibrated by TSI and can be used to measure velocities down to ~0.045 m/s. Figure 14 in APPENDIX C shows the calibration curve for the probe. Accurate data can be obtained over the range of 0.091–1.7 m/s. In addition, an uncertainty analysis in measurement accounting for the possible effect of natural convection on low-velocity measurements was made by TSI for a hot-film anemometer probe similar to that used in this study. The analysis was done for the low-velocity range of 0.03–0.13 m/s, and the result is shown in Fig. 15 in APPENDIX C. This analysis also ap-

plies to the hot-film probe used in this study. The result shows that a velocity measurement of 0.045 m/s would have an uncertainty of ±0.021 m/s (or about ±46%), and as the velocity increases the uncertainty of measurement is drastically reduced such that a measurement of 0.09 m/s would have an uncertainty of only ±0.0128 m/s (or about ±14%).

Once the hot-film anemometer probe was placed at a location for velocity measurement, a personal computer (Apple IIe) connected to the probe recorded 2,048 measurements with an interval between recordings of 6,400 μs for a total recording time of 13.1 s. Longer recording times of 30 s and 1 min were also tested to obtain velocity data at various sections of the nasal cavity model. When compared with the velocity data (and intensity of turbulence) obtained with the recording time of 13.1 s, they showed no significant differences. When the hot-film anemometer probe was inserted into the model, it was rotated to detect the maximum velocity at the point. In most cases, the maximum velocity (U_z) was found to be in the direction perpendicular to the plane of the particular cross section under study. Because the probe cannot resolve individual velocity components, it is really measuring a scalar flow speed ($\mathbf{u} \cdot \mathbf{n}$, where $\mathbf{n}$ is a unit vector
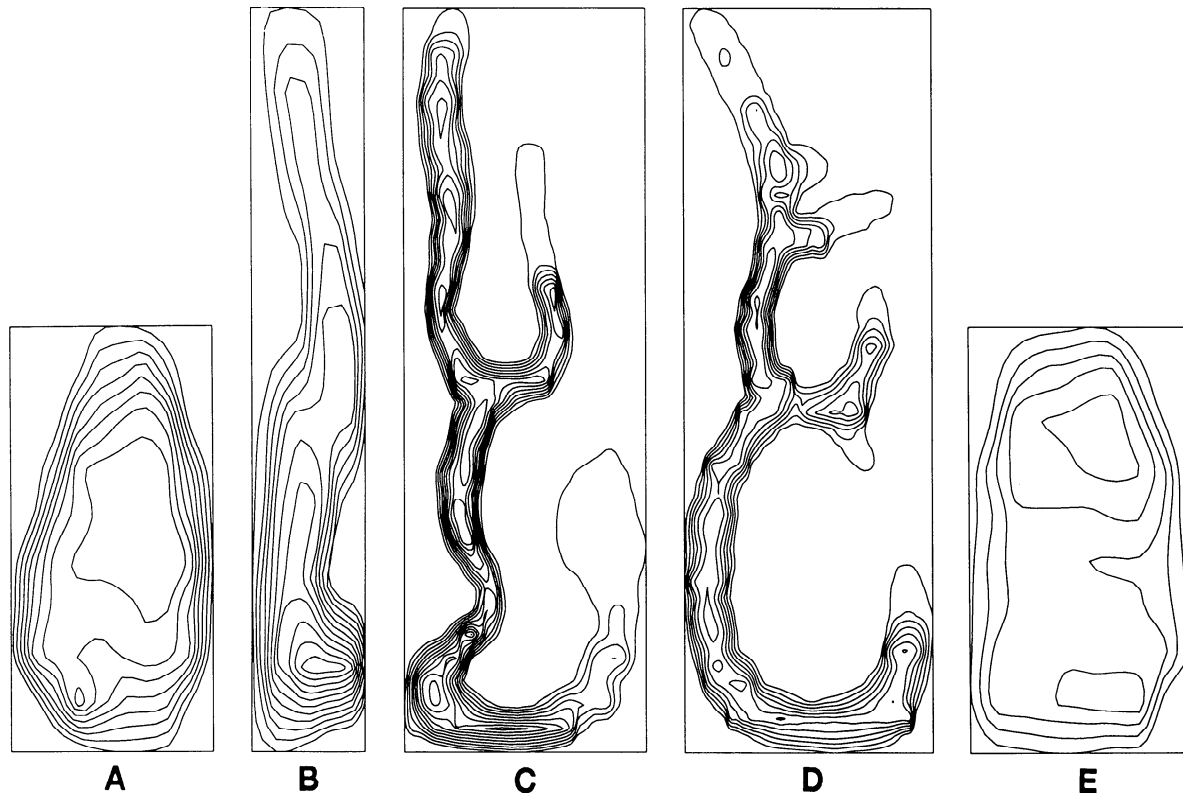
FIG. 6. Isospeed contour maps for high expiratory nasal airflow. U_0 = 15.4 m/s. Distance between lines represents 10% of U_0. A, plane 1; B, plane 2; C, plane 3; D, plane 4; E, plane 5.

normal to the probe) at each measurement point. For this reason, we refer to isospeed contours in the discussion section below. In most cases, the longitudinal velocity component (U_z) is the predominate contributor to $\mathbf{u} \cdot \mathbf{n}$. From these data, a computer program (model 6150, TSI) for statistical analysis calculated the mean velocity and the turbulence intensity of airflow at the point where the measurements were made. This procedure was repeated for all measurement sites throughout the model for all three inspiratory flow rates and one expiratory flow rate of 1,100 ml/s. Measurements were made with and without the simulated nasal hairs present.

To make numerical comparisons of velocity profiles among different measurement locations and different flow rates, each velocity measured was made nondimensional by dividing it by the highest velocity (U_O) measured at the external naris for each flow rate. U_O values for the high, medium, and low inspiratory flows were 0.77, 0.44, and 0.15 m/s, respectively (equivalent to 15.4, 8.8, and 3 m/s, respectively, in the real nose), and that for the high expiratory flow was also 0.77 m/s. All distances across the cross sections at the measurement sites were also made nondimensional by dividing them by the total length between the walls along the probe path at that given site. These nondimensional velocity and measurement location data were then put into a contour plot computer program (Golden Software, Golden, CO) to produce isospeed contour maps for each cross section studied in the model.

RESULTS

The majority of velocity profile points measured for high and medium flow rates were well above the mini-

mum calibration velocity of 0.091 m/s with ±14% uncertainty indicated by the solid line across the velocity profiles in Fig. 17 in APPENDIX C. For the low flow rate, although points closest to the wall were below the minimum velocity of 0.091 m/s, most of the data were >0.045 m/s with ±46% uncertainty indicated by the dashed line in Fig. 17 in APPENDIX C. This means that most velocity points (90% of the data) measured at the low flow rate are reliable within ±46%, even when the possible artifact of natural convection is considered. It is reassuring that the velocity measured at the low flow rate decreased monotonously as the probe approached the wall of the nasal cavity model. This phenomena would not occur if artifact due to natural convection were considerable compared with the forced convection caused by airflow.

The results for the medium inspiratory nasal airflow are shown for the five nasal cross sections in Fig. 4. In Fig. 5, selected isospeed contour maps for high inspiratory flow are compared with corresponding maps for low inspiratory flow. Figure 6 shows the isospeed contour maps for high expiratory nasal airflow.

In Figs. 7 and 8, the normalized cross-sectional velocity profiles for the three inspiratory flows are plotted against the nondimensional cross-sectional distances in plane 1 (naris) and plane 3, respectively. The alphabetically labeled curves in these plots correspond to the measurement locations on the planes shown in Fig. 2. In Fig. 8D the normalized cross-sectional velocity profiles measured in the middle of the olfactory region (labeled as plane 6 in Fig. 2A) for medium inspiratory flow are presented. Figure 9 shows a comparison of the central nasopharyngeal (plane 5D) inspiratory velocity profile measured in this study with that obtained in the study by
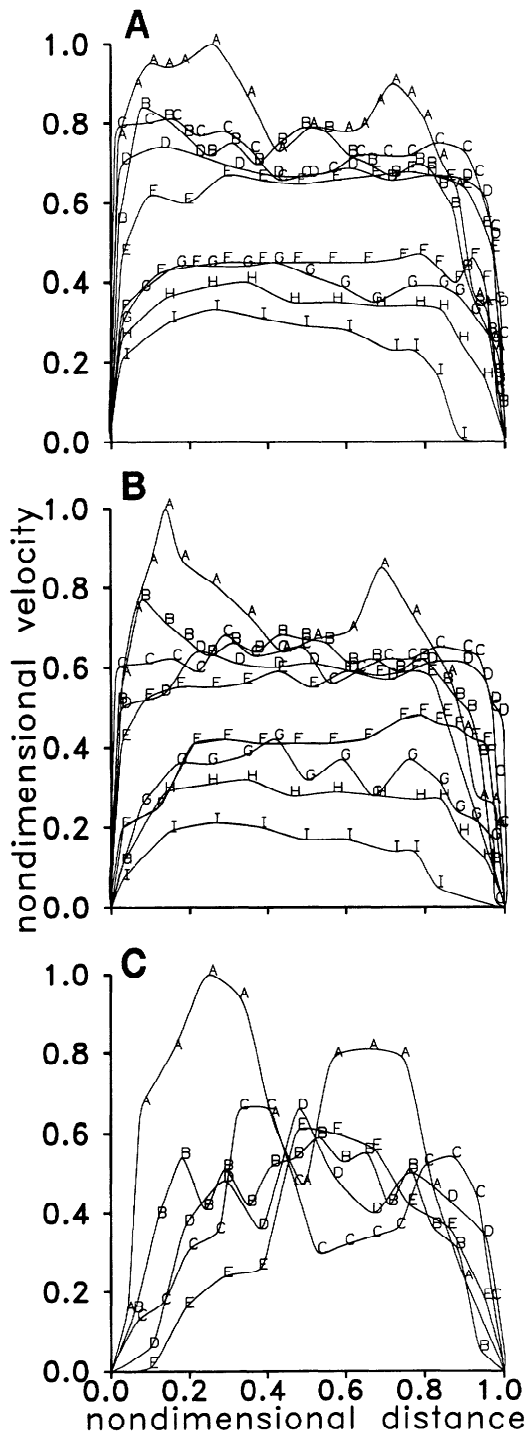
FIG. 7. Normalized cross-sectional velocity profiles at naris (*plane 1*) for high (*A*), medium (*B*), and low (*C*) inspiratory nasal airflow. Velocity measurement points are indicated by letters corresponding to measurement lines shown in Fig. 2.

Girardin et al. (6), who used laser-Doppler velocimetry in a normal size nasal cavity but at a much lower flow rate (167 vs. 560 ml/s).

The longitudinal cross-sectional mean velocity profiles for the inspiratory flow inside the model are compared with those for the expiratory flow at the same flow rate in Fig. 10, *A* and *B*.

Volume-flow distributions throughout the human nasal cavity were obtained by combining the data of velocity and the local area of the cross sections of the nasal cavity from the CAT scans. The average velocity at a given measurement site was calculated from the velocity profile data and was then multiplied by the local area of the cross section to generate the local volume flow. In Fig. 10, *C* and *D*, normalized volume-flow distribution inside the nasal cavity for high inspiratory flow rate is compared with that of the expiratory flow with the same total flow rate. Normalized volume flow distributions for all three inspiratory flows are shown in Fig. 10*C*.

The average values of the intensity of turbulence measured at the naris, the inferior and middle turbinate region, the olfactory region, and the nasopharynx are presented in Fig. 11 for all airflows studied.

Finally, the isospeed contour map and the corresponding cross-sectional velocity profiles for the low inspiratory flow rate at the naris without the nasal hairs are shown in Fig. 12.

DISCUSSION

The nasal passages are responsible for two important physiological functions, respiratory defense and olfaction. Study of nasal airflow patterns is essential for understanding the mechanisms of these functions. As shown in Figs. 4, 5, and 10, the nasal airflow distributions and isospeed contour maps measured at a given nasal cross section are very similar for all inspiratory flow rates. It has been found that ~50% of inspired air flows through the combined middle and inferior airways (see Fig. 1*C*) and ~14% through the olfactory region at all flow rates studied. These results are in contrast to the earlier findings of Stuiver (22), who suggested changes in percent flow through different regions as flow rate is varied. Our results suggest that the trajectories of inhaled air-borne particles and odorant molecules would be similar throughout the nasal cavity regardless of the total inspiratory flow rate. A similar observation has been made by Morgan et al. (13) and confirms the previously reported (20) preliminary results obtained in the same model. For investigation of the absorption of inhaled molecules onto the nasal cavity walls and to determine the pressure drops or nasal resistance associated with the flow rates, it is desirable to determine whether the nasal airflow is laminar or turbulent.

The onset of turbulence in airflow, or the transition from laminar to turbulent flow, is related to Re, $(\rho\bar{u}d)/\mu$, which may be interpreted physically as the ratio of inertial forces to viscous forces in the flow, where ρ is the density of air, μ is the dynamic viscosity of air, and d is here taken to be the cross-sectional distance between the two nasal walls determined from the CAT scans (see Table 2 in APPENDIX A). At Re greater than ~2,000, most steady flows in closed conduits become unstable, which means that any small disturbance in the flow will tend to become larger and the laminar velocity profile will be drastically altered by the growth of turbulent eddies (28). The local Re (based on local airway diameter) calculated for the medium sniff flow rate inside the real nasal cavity or the model range from 250 in the olfactory region to 4,500 in the inferior airway. The Re is not the sole criterion for predicting the onset of turbulence. If air flows through a diverging conduit such as the nasal valve, a transition to turbulent flow can take place at an Re con-
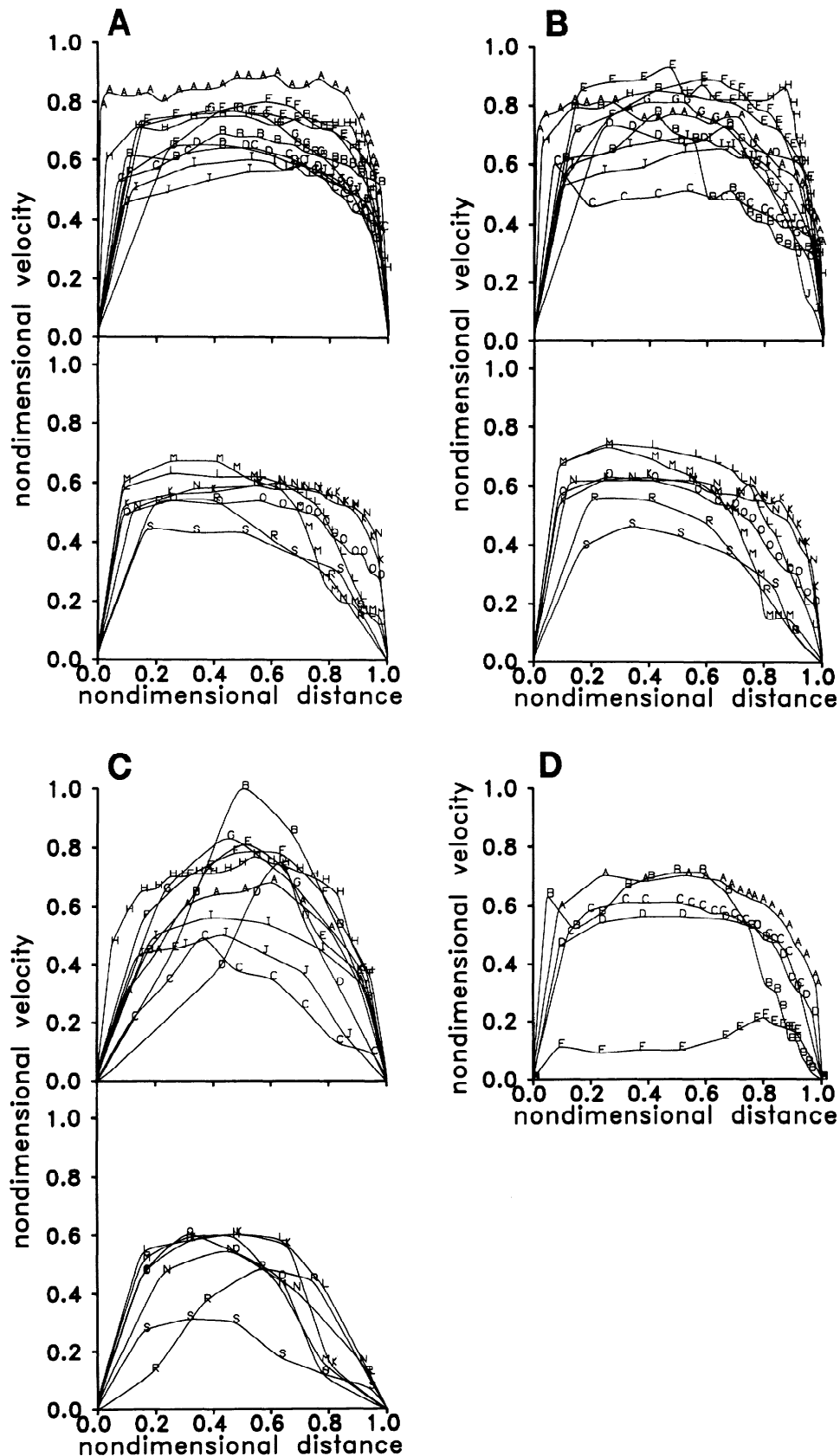
FIG. 8. Normalized cross-sectional velocity profiles at *plane 3* for high (*A*), medium (*B*), and low (*C*) inspiratory nasal airflow and in the olfactory region (*plane 6*) for medium inspiratory flow (*D*). Velocity measurement points are indicated by letters corresponding to measurement lines shown in Fig. 2.

siderably below the critical value of 2,000 (29). When flow in tubes becomes turbulent, the drag force that the fluid exerts on the tube walls increases sharply (28), and the turbulent core makes the velocity profiles relatively flat at the tube center and steep near the tube walls.

From the local Re, the shapes of the velocity profiles shown in Figs. 7 and 8, the intensity of turbulence shown in Fig. 11, and the point velocity recordings shown in APPENDIX B, the airflow inside the model and in the real nasal cavity appears to be mostly turbulent for airflows
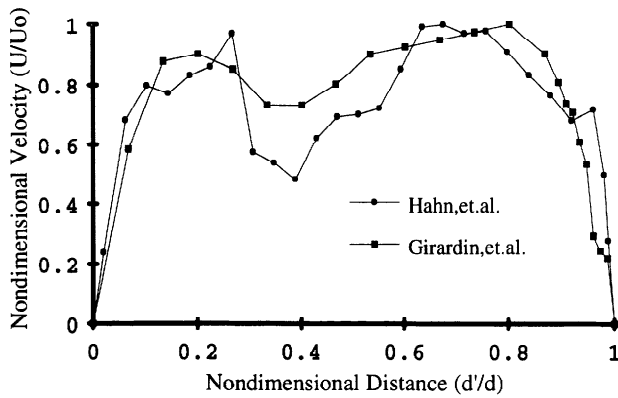
FIG. 9. Normalized velocity profile measured across 1 cross section of nasopharyngeal entrance (*plane 5D*) compared with that obtained by Girardin et al. (6), who used laser-Doppler velocimetry. Study by Girardin et al. is for inspiratory nasal airflow with flow rate of 167 ml/s and $U_0 = 2.05$ m/s in real human nasal cavity. In this study, nasal inspiratory flow rate is 560 ml/s and $U_0 = 0.44$ m/s.

with high and medium flow rate and disturbed laminar flow for the lowest flow rate. These findings are also supported by the insensitivity of the shapes of the normalized flow profiles, shown in Fig. 10C, to the total flow rate of nasal airflow. If the flow in a conduit is laminar, the viscous forces in the flow cause the velocity profiles to exhibit considerable change with increasing flow rate as the onset of turbulence is approached. These recordings show random fluctuations in velocity that are characteristic of turbulent flow. The inspiratory velocity profile measured at the nasopharyngeal entrance in this study and that measured by Girardin et al. (6), using laser-

Doppler velocimetry in a normal size nasal cavity and a lower flow rate (167 ml/s), are very similar, as shown in Fig. 9. This agreement supports the validity of the low-velocity measurements made by the hot-film anemometer probe in this study. Girardin et al. also suggested that the nasal airflow was turbulent. As shown in Fig. 8D, the velocity profiles in the olfactory region are similar to those in the main nasal cavity. It should be noted that the velocity profiles for inspiratory airflow with the lowest flow rate (see Fig. 8C) appear to be less turbulent and more laminar-like with less steep slopes near the walls. Changes in the velocity profiles between the highest and lowest flow rates suggest that, for normal resting breathing, laminar-like flow may be present in much of the nasal cavity. This point remains to be further investigated.

Further evidence of turbulence in nasal airflow is presented in Fig. 13 in APPENDIX B. A time-dependent velocity measurement for inspiratory flow inside the nasal cavity model (*plane 3H*) taken at the high flow rate (Fig. 13B in APPENDIX B) is compared with a measurement taken in front of the fan outside the model (Fig. 13A in APPENDIX B) at the same flow rate. It is apparent that airflow inside the nasal cavity has many more random fluctuations in velocity than airflow generated by the fan alone. A similar comparison of the time-dependent velocity measurements at the low flow rate in front of the fan alone and during inspiration in the nasal cavity has been made in Fig. 13; C and D, in APPENDIX B. They show similar differences in random fluctuations. These measurements provide evidence that nasal airflows are generally turbulent and that any disturbance generated by the
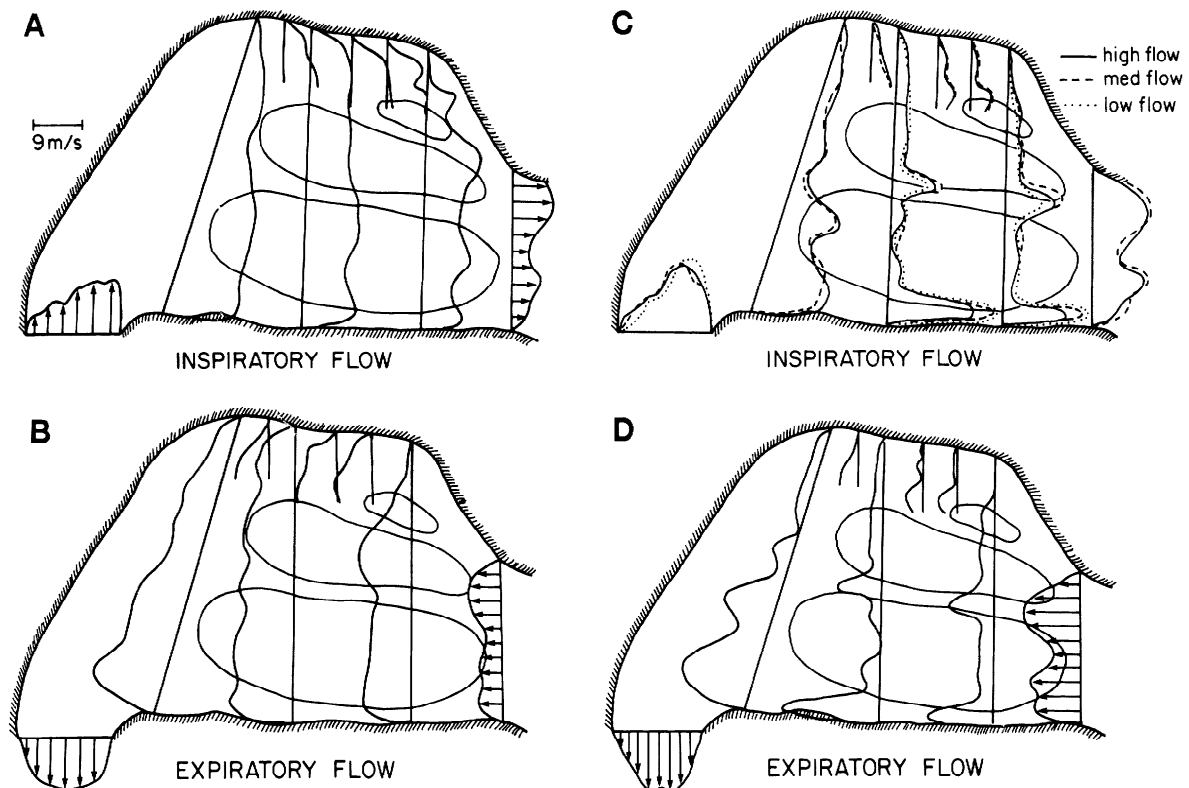

FIG. 10. Longitudinal mean velocity profiles for high inspiratory nasal airflow (A) compared with those for high expiratory nasal airflow (B). Normalized volume-flow distribution profiles inside nasal cavity for high inspiratory flow (C) are compared with those for expiratory flow with same flow rate (D). In C, normalized volume-flow distribution profiles for all inspiratory flows studied are presented. They show little change with total flow rates.
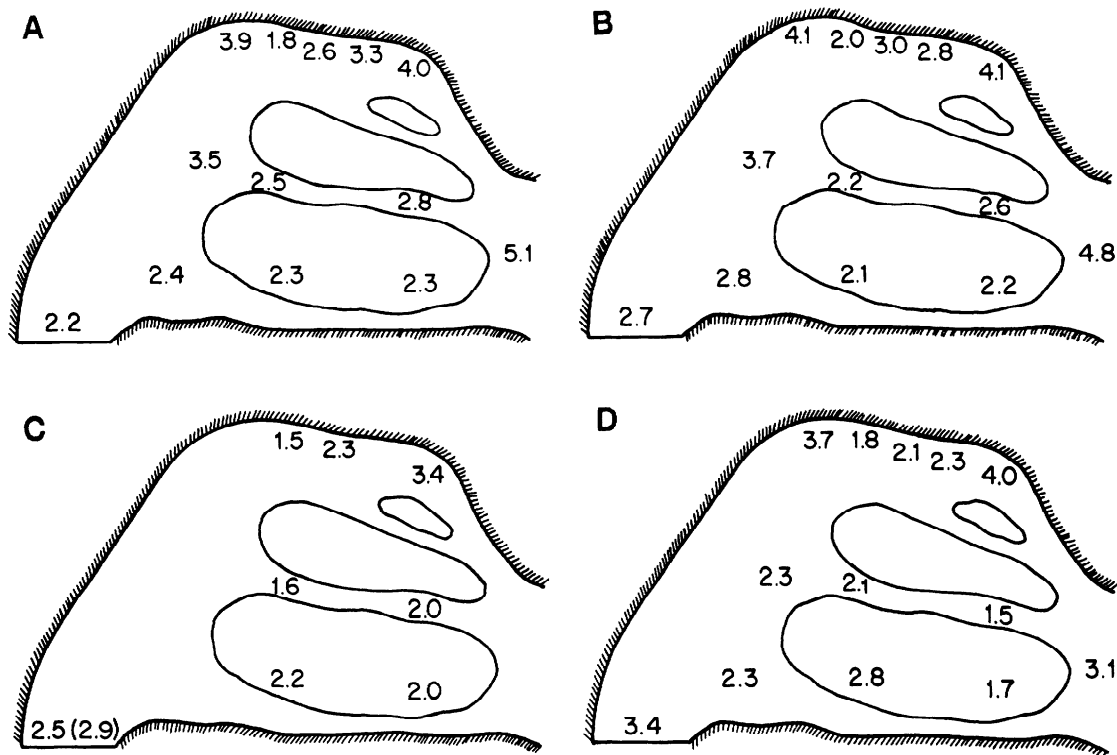
FIG. 11. Intensities of turbulence are shown throughout nasal cavity for high (A), medium (B), and low (C) inspiratory nasal airflow and for high expiratory airflow (D). For low inspiratory flow rate, average values of intensities of turbulence measured at naris with and without nasal hairs are 2.9 and 2.5%, respectively.

fan does not contribute significantly to the turbulence (or randomness) in the nasal airflow for all flow rates studied.

For turbulent flow, the velocity can be expressed in terms of $\bar{u}$ plus a fluctuating component, u', as

$$u = \bar{u} + u' \qquad (3)$$

The intensity (I) of turbulence is defined as

$$I = 100 \frac{\sqrt{(u')^2}}{\bar{u}} \% \qquad (4)$$

and is used as a convenient measure of the magnitude of the turbulent fluctuations (28). There can also be fluctuations in a laminar flow caused by vibration in the pump or fan producing the flow, but if the flow is truly laminar, these will tend to die out because of viscous dissipation of energy. The hot-film anemometer has proved to be an effective method for the measurement of turbulence (27). The probe used in this experiment has a frequency response time of $\sim 10^{-5}$ s (25). The intensity of turbulence for airflows inside the nasal cavity for all flow rates studied is presented in Fig. 11. The regional differences in the magnitudes of the intensity of turbulence are consistent for all flow rates. As shown in Fig. 11, C and D, the intensities of turbulence in the turbinate region and olfactory region for the lowest inspiratory flow and expiratory flow are slightly lower than those for the medium and high inspiratory flows. Turbulence is intensified when the airflow is forced to change its direction by sudden expansion or curving of the airway, and this may account for generally higher values for the intensities of turbulence measured near the nasal valve and in the nasopharynx for all

flow rates. For most turbulent flows the intensity of turbulence ranges from ~ 1 to 10% (26, 28). Our results suggest that the airflow inside the nasal cavity model is moderately turbulent at most physiological flow rates.

The measured velocity profiles can be used to obtain the total shear stress, τ_0, exerted by airflow on the nasal walls. τ_0 can be expressed as a combination of the laminar (or viscous) shear stress, τ_l, due to pure molecular momentum transfer, and the Reynolds stress, τ_t, the contribution to the total shear stress by the turbulent fluctuations (2) as

$$\tau_0 = \tau_l + \tau_t \qquad (5)$$

τ_l is defined as

$$\tau_l = \mu \frac{d\bar{u}}{dy} \qquad (6)$$

and τ_t can be written in an analogous form as

$$\tau_t = \rho \overline{u'v'} = \mu_t \frac{d\bar{u}}{dy} = \rho\varepsilon \frac{d\bar{u}}{dy} \qquad (7)$$

where $d\bar{u}/dy$ is the mean velocity gradient, μ_t is the eddy viscosity, ε is the eddy diffusivity, and u' and v' are the turbulent fluctuations in the x- and y-direction, respectively. In laminar and turbulent flow, all velocity components vanish at stationary solid walls (no slip condition) and turbulent components are very small in the immediate neighborhood of the wall (21). It follows that the only stresses that act very near the wall are the viscous stresses and that in every turbulent flow there exists a very thin layer next to the wall that, in essence, behaves like one in laminar motion without any turbulence. This
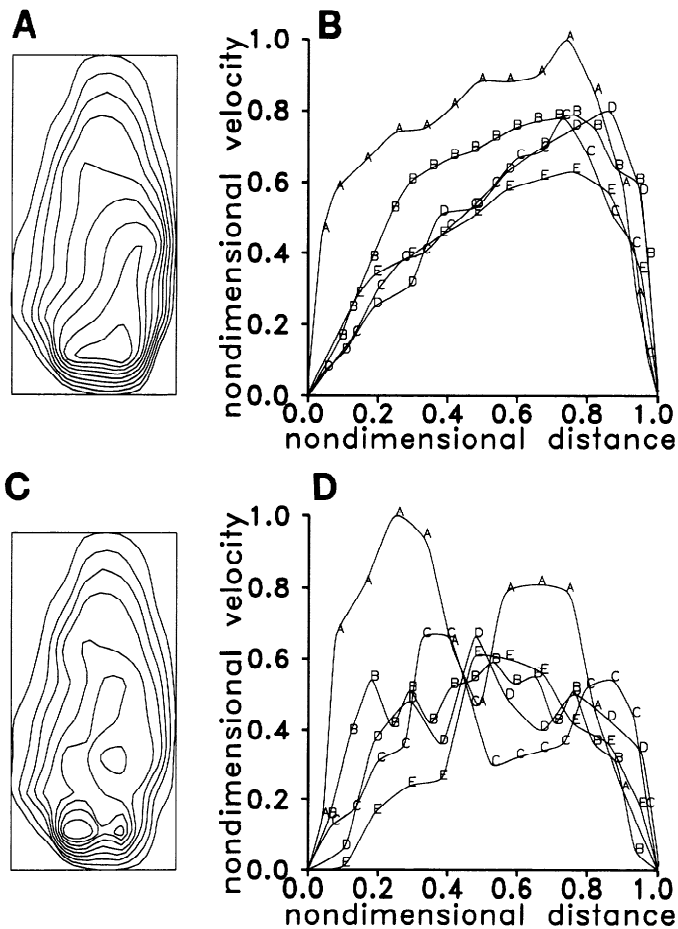
FIG. 12. *A*: isospeed contour map for low inspiratory airflow at naris without nasal hairs. *B*: corresponding cross-sectional velocity profiles normalized by $U_0 = 3.58$ m/s. They are compared with isospeed contour map (*C*) and corresponding cross-sectional velocity profiles (*D*) for naris with nasal hairs. Average values of intensities of turbulence measured at naris with and without nasal hairs are 2.9 and 2.5%, respectively.

is known as the laminar sublayer, and the velocity increases linearly with distance from the wall within this layer (9).

In fully developed turbulent flow, the laminar sublayer joins a transitional layer in which the turbulent velocity fluctuations start to give rise to turbulent shear stresses that are comparable with the viscous stresses. At still larger distances from the wall, the turbulent stresses eventually completely dominate as the turbulent boundary layer merges with the turbulent core. The thickness of the laminar sublayer is, in most cases, very small such that it is difficult to measure experimentally (21). For

TABLE 1. *Pressure drop in the human nasal cavity*

Flow Rate, ml/s	Calculated ΔP, cmH$_2$O	Measured ΔP^*, cmH$_2$O
1,100	4.5	6.0–17
560	2.3	1.5–4.3
180	0.4	0.26–0.74

Pressure drop (ΔP) inside human nasal cavity for 3 inspiratory flow rates is estimated using average total shear stress at central nasal cavity wall calculated from velocity gradients measured near the wall. Our results agree well with the range of ΔP^* for same nasal flow rates measured in human subjects by Sullivan and Chang (23).

TABLE 2. *Dimensions of human nasal cavity used in model study*

	Plane 1	Plane 2	Plane 3	Plane 4	Plane 5	Plane 6
Perimeter, mm	53	82	181	162	63	
Cross-sectional area, mm^2	173	135	145	162	258	
Cross-sectional distance, mm						
A	6.3	5.2	10	10.1	12	1.5
B	8.4	4.9	2.7	2.1	14.1	1.5
C	7.5	4.0	1.7	2.5	13.9	1.8
D	5.4	3.8	1.2	2	10.1	1.7
E	5.2	4.0	1.7	2.3	12.9	1.8
F	5.6	4.6	1.5	2.5	12.1	1.7
G	5.7	4.7	1.7	4.7	10.5	
H	4.6	3.8	4.7	1.7	8.8	
I	4.2	3.4	1.7	1.5	5.7	
J		2.7	1.0	1.7		
K		2.5	1.7	5.2		
L		2.6	1.6	3.1		
M		2.3	1.6	2.3		
N		2.1	1.5	2.0		
O		1.7	1.5	1.7		
P			2.3	2.3		
Q			3.8	1.5		
R			1.3			
S			1.2			

fully developed turbulent flow inside pipes, the thicknesses of the laminar sublayer (δ_l) and the turbulent boundary layer (δ_t) have been estimated from the universal velocity distribution law (21) as

$$\delta_l = 5 \frac{\nu}{u^*} \qquad (8)$$

and

$$\delta_t = 70 \frac{\nu}{u^*} \qquad (9)$$

with the friction velocity at the wall, u^*, defined as

$$u^* = \sqrt{\frac{\tau_0}{\rho}} \qquad (10)$$

The above equations show that the turbulent boundary layer is much thicker than the laminar sublayer and that neither thickness can be determined without knowing τ_0. We can roughly estimate τ_0 from Blasius' correlation (21) for the wall shear stress in a fully developed turbulent flow through a pipe

$$\tau_0 = 0.03955 \rho \bar{u}^{1.75} \nu^{0.25} d^{-0.25} \qquad (11)$$

By using $\bar{u} = 27$ cm/s, $\rho = 0.0013$ g/cm^3, $\nu = 0.15$ cm^2/s, and $d = 10$ cm for airflow at the medium flow rate through the nasal cavity model, u^* can be estimated from *Eqs. 10* and *11* to be $\sim$2.1 cm/s. Consequently, from *Eq. 8*, δ_l would be $\sim$3.6 mm. In his mixing length theory for turbulent flow, Prandtl (in Ref. 27) introduced the assumption [reasonably well justified experimentally (9)] that the shear stress remains constant across the tube, i.e., that
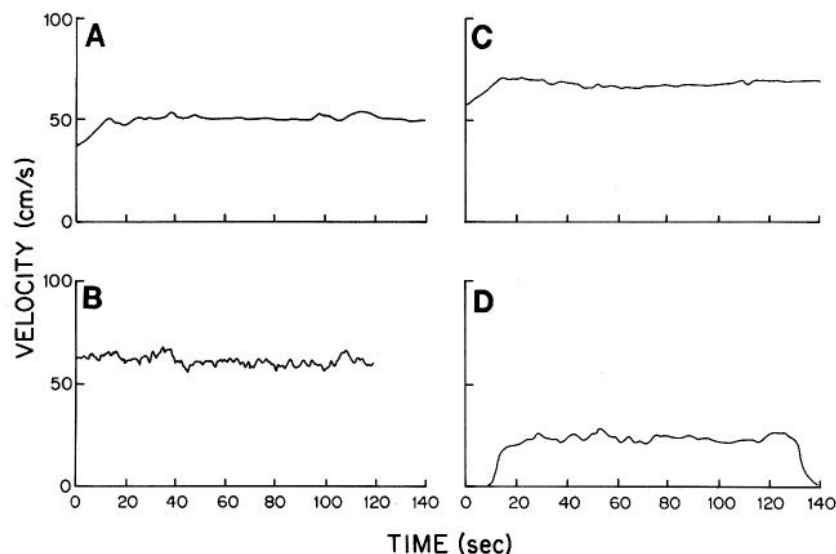
FIG. 13. Time-dependent velocity recordings.

$$\tau_t = \tau_0 \qquad (12)$$

If *Eqs. 4, 7, 10,* and *12,* are combined and if it is assumed that the magnitudes of u' and v' are similar, u^* can be written as

$$u^* = \sqrt{\frac{\tau_t}{\rho}} = \sqrt{(u')^2} = \frac{I\bar{u}}{100} \qquad (13)$$

The above arguments hold for fully developed turbulent flow inside a straight tube of constant diameter. They are used here only as a guideline for approximation of the more complex flow patterns inside the human na-

sal cavity. For airflow through the model at the medium flow rate, the average value of u^* calculated from I and $\bar{u}$ measured near the wall is ~1.5 cm/s and the thickness of the laminar sublayer can be estimated from *Eqs. 8* and *13* to be ~5 mm. Neither of the above analyses can give the exact value of the viscous sublayer thickness for airflow inside the nasal cavity model; however, they can provide an approximation of it.

In our experiments, the velocity measurements closest to the wall were made, in most cases, within 2 mm so that, according to the above estimates, they are likely to be well inside the turbulent boundary layer and even in-
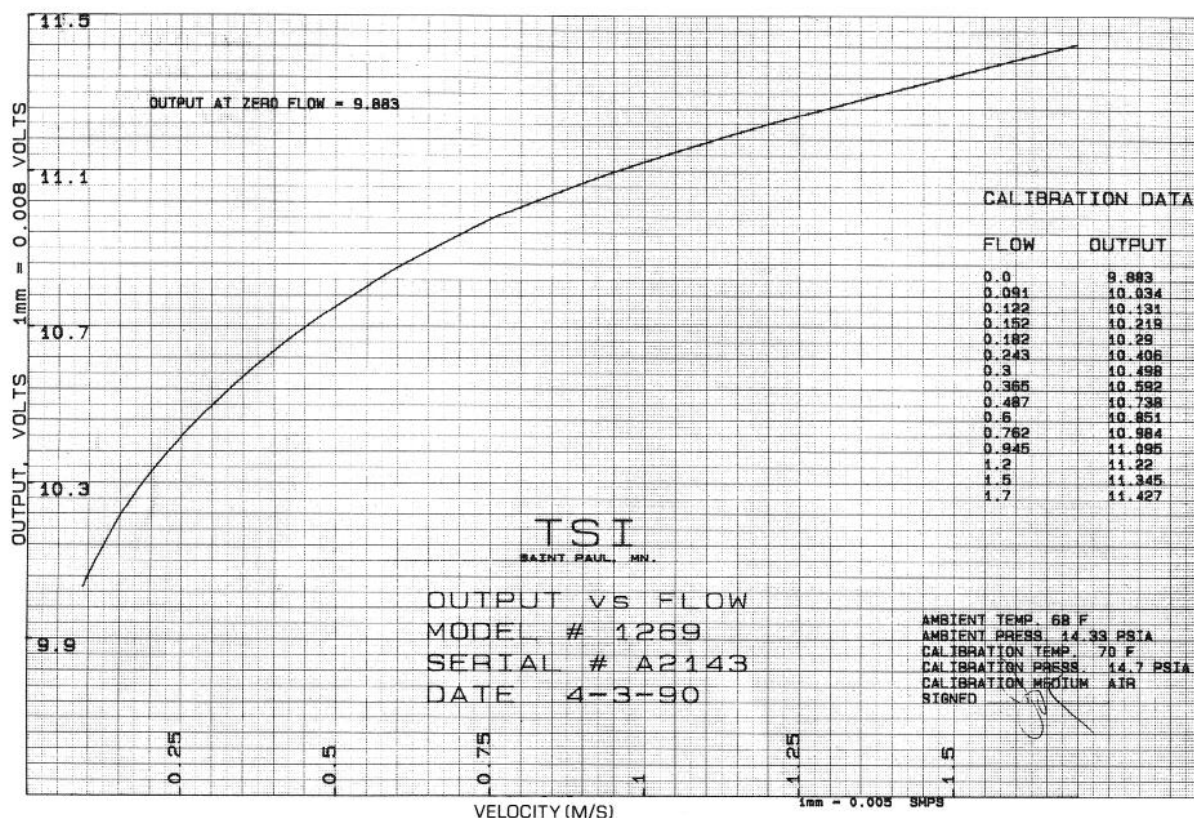

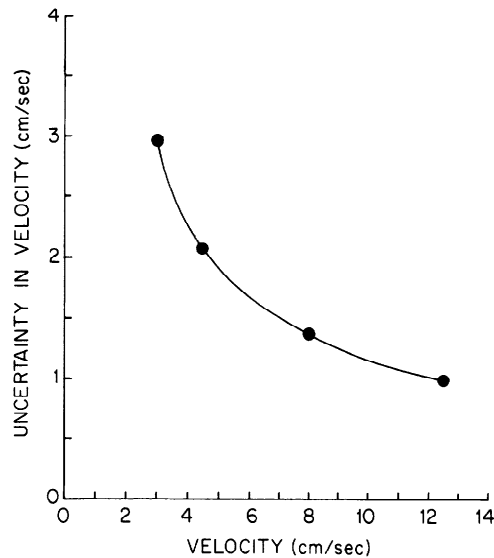FIG. 14. Calibration curve for hot-film anemometer probe. [From TSI (St. Paul, MN).]

FIG. 15. Uncertainty in low-velocity measurements by hot-film anemometer probe.

side the laminar sublayer. The velocity profiles measured near the walls have very steep and nearly constant slopes, as shown in Figs. 7 and 8, such that the slopes, which are predicted by theory to be constant within the laminar sublayer, should provide good estimations of the velocity gradients there.

As an example of the application of the velocity profiles to the calculation of other nasal transport properties, we estimated the pressure drop through the human nose on the basis of the measured velocity gradients at the wall, $\left.\dfrac{d\bar{u}}{dy}\right|_{y=0}$. For steady flows inside straight tubes of constant cross section, the pressure drop, ΔP, along a tube length, L, is related to the total shear stress, exerted by the flow on the tube wall (9) as

$$\Delta P = \frac{4\tau_0 L}{D_h} \qquad (14)$$

where D_h is the hydraulic diameter [(4 × cross-sectional area)/perimeter]. The pressure drops inside the human nose for three inspiratory flow rates were estimated from *Eq. 14* by using the average values of τ_0 calculated for each flow rate from our velocity gradients at the nasal wall in the central nasal cavity. Although *Eq. 14* is derived for tubes of constant cross section and although ΔP calculated for the nasal cavity from *Eq. 14* can only be an estimate, our results show good agreement with the range of ΔP for the same nasal flow rates measured experimentally in human subjects by Sullivan and Chang (23) (Table 1). The poorer agreement for the highest flow rate is probably because of a lack of collapse of the nasal valve region in the model.

In Fig. 12, the isospeed contour map and the corresponding cross-sectional velocity profiles for the low inspiratory flow at the naris with and without nasal hairs are shown. It is clear that the contour map is more complex and the velocity profile more disturbed near the nares for airflow inside the model with nasal hairs than the model without nasal hairs. The average values of the intensities of turbulence for the same low inspiratory
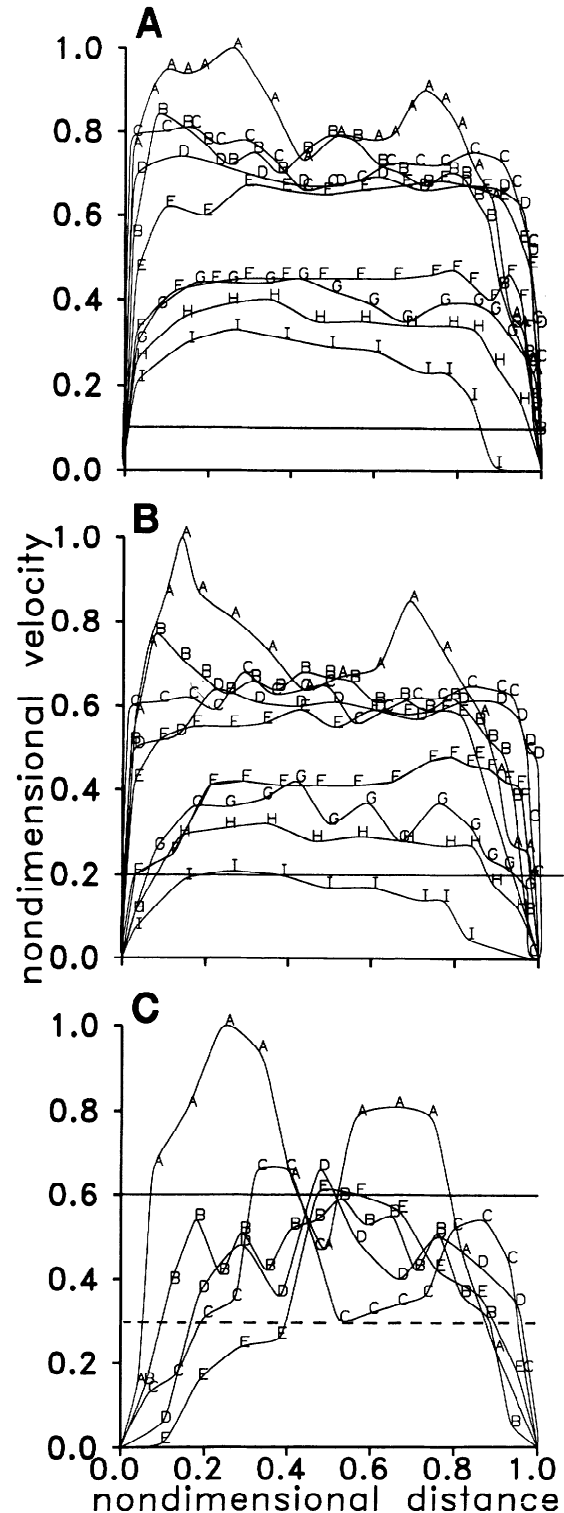
flow rate measured at the nares with and without nasal hairs are ~2.9 and 2.5%, respectively, as shown in Fig. 11C. It would seem that on inspiration nasal hairs are responsible for slightly higher turbulence in the external nares. Measurements in the model show that velocity profiles downstream from the naris in the turbinate and olfactory regions are little affected by the presence of the hairs.

FIG. 16. Low limit of velocity measurement using hot-film probe for high (*A*), medium (*B*), or low (*C*) inspiratory nasal airflow.

Although the large scale nasal cavity model is anatomically correct, it lacks warm moist walls that may cause thermal buoyancy effects inside the real nose. To estimate the possible effect of thermal buoyancy on velocity profiles in nasal airflow, it is necessary to examine the Grashof number, Gr, and the Prandtl number, Pr, defined (3) as

$$Gr = g\beta \frac{(T_w - T_\infty)x^3}{\nu^2} \qquad (15)$$

and

$$Pr = \mu \frac{C_p}{k} \qquad (16)$$

where g is the gravitational constant, β is the coefficient of thermal expansion, x is the tube diameter, k is the thermal conductivity, C_p is the heat capacity of air, and T_W and T_∞ are the temperatures at the wall and in the airflow far from the wall inside the nasal cavity, respectively. For airflow inside a tube of equivalent diameter to the normal healthy nose, Gr (with $T_W = 32°C$ and $T_\infty = 26°C$) and Pr are estimated to be ~630 and 0.71, respectively. For these values and for Re ranging from 300 to 4,500, it has been empirically determined that forced convection effects are dominant and that natural convection effects are negligible near the heated surface (3, 12). This suggests that the effect of thermal buoyancy on the nasal airflow velocity profiles would be small. Similar considerations apply to the effect of water vapor evaporation on the nasal airflow velocity profiles. If a complete heat and mass transfer analogy is assumed, mass transport of water should also have a very small effect on the velocity profiles of nasal airflow.

Airflow inside the real nose is not in steady state; i.e., it decelerates and accelerates to and from rest in normal breathing or sniffing. The importance of the unsteadiness of nasal airflow can be estimated by examining α, discussed previously, and the Strouhal number, S, defined as

$$S = \frac{2\pi\omega d}{\bar{u}} \qquad (17)$$

For a typical diameter of the real nasal airway ($d = 0.5$ cm), breathing frequency of 2 s^{-1}, and the average velocity of 5.4 m/s for the medium nasal airflow rate, S and α for nasal airflow are estimated to be ~0.01 and 4.5, respectively. Although the value of α suggests that unsteadiness may be of some importance, the low value of S suggests that it is not. Other investigators (4, 23) have also concluded that under most conditions nasal airflow can be considered as steady or quasi-steady.

Shortcomings of the present nasal cavity model include lack of mucus on the walls and lack of flexibility so that the active movement of the real nasal wall, as in constriction or collapse of the nasal valve in vigorous sniffing, is missing. Also, the straight cylindrical aluminum foil duct used for housing the fan does not properly simulate the curvature of the human nasopharynx. This may have affected the expiratory flow profiles, and these features remain to be included in future studies.

APPENDIX A

The dimensions (cross-sectional area, distance, and perimeter) of the human nasal cavity used in the model study are presented in Table 2. The large-scale model of the human nasal cavity has dimensions that are 20 times greater than those in Table 2.

APPENDIX B

The time-dependent velocity recordings for the airflow generated by the fan alone used in the nasal cavity model are compared with those for the airflow inside the model. Figure 13, A and C, shows the time-dependent velocity measurements obtained in front of the fan producing the airflow with the high (1,100 ml/s) and low (180 ml/s) flow rates, respectively. These measurements are compared with the time-dependent velocity measurements made for the airflow inside the nasal cavity model with the same flow rates in Fig. 13, B and D, for high and low flow rates, respectively. It is shown that the airflow generated by the fan alone has very little noise or random fluctuations. The airflow inside the nasal cavity model, on the other hand, has noticeably more random fluctuations for both high and low flow rates.

APPENDIX C

The calibration curve for the hot-film anemometer probe (model 1269, TSI) used in this study is shown in Fig. 14. The minimum velocity that can be measured with confidence and with uncertainty of ±14% is 0.091 m/s. In Fig. 15, the result of the uncertainty analysis of the hot-film anemometer probe accounting for the possible effect of natural convection in low-velocity measurement is presented. The result suggests that a velocity measurement of 0.045 m/s would have the uncertainty of ±0.021 m/s or about ±46%. As the velocity increases, the uncertainty of measurement is drastically reduced, such that a measurement of 0.09 m/s would have the uncertainty of only ±0.0128 m/s or about ±14%. These velocity limits are indicated by lines (solid for 0.091 m/s, dashed for 0.045 ± 0.021 m/s) across the velocity profiles for all flow rates shown in Fig. 16. Most of the velocities measured for high and medium flow rates are well above the minimum calibration velocity of 0.091 m/s, and most of the velocity data (90%) for low flow rate are above 0.045 m/s.

REFERENCES

1. BEIDLER, L. M. Effect of odor flow rate on olfactory response. *Federation Proc.* 17: 12, 1958.
2. BIRD, R. B., W. E. STEWART, AND E. N. LIGHTFOOT. *Transport Phenomena.* New York: Wiley, 1960.
3. BURMEISTER, L. C. *Convective Heat Transfer.* New York: Wiley, 1983.
4. CHANG, H. K. Flow dynamics in the respiratory tract. In: *Respiratory Physiology, an Analytical Approach,* edited by H. K. Chang and Manuel Paiva. New York: Dekker, 1989, p. 57–138.
5. ECCLES, R. The central rhythm of the nasal cycle. *Acta Otolaryngol.* 86: 464–468, 1978.

6. GIRARDIN, M., E. BILGEN, AND P. ARBOUR. Experimental study of velocity fields in a human nasal fossa by laser anemometry. *Ann. Otol. Rhinol. Laryngol.* 92: 231–236, 1983.

7. GOODALE, J. L. An experimental study on the respiratory functions of the nose. *Boston Med. Surg. J.* 135: 457–487, 1986.

8. HORNUNG, D. E., D. A. LEOPOLD, S. L. YOUNGENTOB, P. R. SHEEHE, G. M. GAGNE, F. D. THOMAS, AND M. M. MOZELL. Airflow patterns in a human nasal model. *Arch. Otol. Head Neck Surg.* 113: 169–172, 1987.

9. KUNDU, P. K. *Fluid Mechanics.* San Diego, CA: Academic, 1990, p. 416–473.

10. LEOPOLD, D. A. Relation between nasal anatomy and function. In: *Clinical Measurement of Taste and Smell,* edited by H. L. Meiselman and R. S. Rivlin. New York: Macmillan, 1986, p. 529–549.

11. MASING, H. Investigations about the course of flow in the nose model. *Arch. Klin. Exp. Ohren. Nasen. Kehlkopfheilkd.* 189: 371–381, 1967.

12. METAIS, B., AND E. R. G. ECKERT. Regimes of free, forced, and mixed convection for flow through horizontal tubes. *Trans. ASME J. Heat Trans.* 86: 295–296, 1964.

13. MORGAN, K. T., J. S. KIMBELL, T. M. MONTICELLO, A. L. PATRA, AND A. FLEISHMAN. Studies of inspiratory airflow patterns in the nasal passages of the F344 rat and rhesus monkey using nasal molds: relevance to formaldehyde toxicity. *Toxicol. Appl. Pharmacol.* 110: 223–240, 1991.

14. OTTOSON, D. Analysis of the electrical activity of the olfactory epithelium. *Acta Physiol. Scand. Suppl.* 122: 1–83, 1956.

15. PARKER, C. A. Some observations and remarks on the air currents in nasal respiration. *J. Laryngol. Rhinol. Otol.* 16: 345–355, 1901.

16. PATRA, A. L., A. GOOYA, AND K. T. MORGAN. Airflow characteristics in a baboon nasal passage cast. *J. Appl. Physiol.* 61: 1959–1966, 1986.

17. PROCTOR, D. F., AND J. C. F. CHANG. Comparative anatomy and physiology of the nasal cavity. In: *Nasal Tumors in Animals and Man,* edited by G. Reznik and J. F. Stinson. Boca Raton, FL: CRC, 1983, vol. 1, p. 1–33.

18. PROETZ, A. W. *Applied Physiology of the Nose* (2nd ed.). St. Louis, MO: Annals, 1953.

19. PROETZ, A. W. Air currents in the upper respiratory tract and their clinical importance. *Ann. Otol. Rhinol. Laryngol.* 60: 439–467, 1951.

20. SCHERER, P. W., I. HAHN, AND M. M. MOZELL. The biophysics of nasal airflow. In: *The Otolaryngologic Clinics of North America,* edited by C. P. Kimmelman. Philadelphia, PA: Saunders, 1989, vol. 22, p. 265–278.

21. SCHLICHTING, H. *Boundary-Layer Theory.* New York: McGraw-Hill, 1979.

22. STUIVER, M. *Biophysics of the Sense of Smell* (PhD thesis). Groningen, The Netherlands: Rijks University, 1958.

23. SULLIVAN, K. J., AND H. K. CHANG. Steady and oscillatory transnasal pressure-flow relationships in healthy adults. *J. Appl. Physiol.* 71: 983–992, 1991.

24. SWIFT, D. L., AND D. F. PROCTOR. Access of air to the respiratory tract. In: *Respiratory Defence Mechanisms,* edited by J. D. Brain, D. F. Proctor, and L. M. Reid. New York: Dekker, 1977, p. 63–93.

25. TSI. *Instruction Manual for TSI Anemometer Probe #1269.* St. Paul, MN: TSI, 1987.

26. TSI. *Measurements in Turbulent Flows of Low Intensity.* St. Paul, MN: TSI, 1990. (Tech. Bull. 13)

27. WELTY, J. R., C. E. WICKS, AND R. E. WILSON. *Fundamentals of Momentum. Heat and Mass Transfer.* New York: Wiley, 1984.

28. WHITAKER, S. *Introduction to Fluid Mechanics.* Malabar, FL: Krieger, 1968.

29. YIH, C. S. *Fluid Mechanics.* Ann Arbor, MI: West River, 1979.